ASME Journal of Turbomachinery
Online journal at:
https://asmedigitalcollection.asme.org/turbomachinery

Impact of Trailing Edge Damage on Nozzle Guide Vane Aerodynamic Performance

Zelimhan Raduev
Department of Engineering Science,
University of Oxford,
Oxford OX2 0ES, UK
e-mail: zelimhan.raduev@eng.ox.ac.uk

Dougal Jackson
Rolls-Royce plc,
WH88, PO Box 3,
Filton BS34 7QE, UK
e-mail: dougal.jackson@rolls-royce.com

Nafiz Chowdhury
Department of Engineering Science,
University of Oxford,
Oxford OX2 0ES, UK
e-mail: md.chowdhury@eng.ox.ac.uk

Thomas Povey[1]
Department of Engineering Science,
University of Oxford,
Oxford OX2 0ES, UK
e-mail: thomas.povey@eng.ox.ac.uk

In this paper, we consider the impact of trailing edge burn-back on the aerodynamic performance of cooled transonic high-pressure nozzle guide vanes. We consider four levels of burn-back ranging from new parts to severely damaged parts. High-fidelity experimental aerodynamic performance data were taken in the Engine Component AeroThermal facility at the University of Oxford, at engine-matched conditions of Mach number, Reynolds number, and coolant-to-mainstream pressure ratio. Experimental data are compared to the results of computational fluid dynamics simulations to provide further insights into the mechanisms affecting performance. We find that for fixed row pressure ratio, increasing burn-back leads to: both increased loading, and increased forward loading; increased film cooling flow due to reloading and increased trailing edge flow due to slot area increase; increased overall boundary layer loss; a significant increase in exit secondary kinetic energy associated with newly formed counterrotating vortices at the edges of the burn-back region; and increased variation in exit whirl angle. We quantify these effects and consider implications for whole-life engine performance. [DOI: 10.1115/1.4067930]

Keywords: computational fluid dynamics (CFD), fluid dynamics and heat transfer phenomena in compressor and turbine components of gas turbine engines, measurement techniques, turbine blade and measurement advancements, turbomachinery blading design, vortex shedding, turbine component erosion

1 Introduction

In operational engines, transonic high-pressure (HP) nozzle guide vanes (NGVs) are subject to trailing edge (TE) erosion and oxidation damage (or, so-called, *burn-back*). Loss of TE material changes the aerodynamic loading of the vane and can significantly change the aerodynamic performance of the row and stage. To build whole-life engine models, the aerodynamic consequences of TE damage need to be both understood and quantified.

Sjolander et al. [1] investigated the aerodynamics of uncooled turbine blades with simulated TE damage in a low-speed linear cascade ($\mathrm{Re} = 3 \times 10^5$, $\mathrm{M} = 0.5$, and $\mathrm{Tu} = 0.3\%$) with flow incidence angles ranging from −10 to +15 deg. Area traverse measurements were taken two-fifths of an axial chord length downstream of the TE. The blades were arranged so that an individual damaged blade (semicircle cut-outs with depths equal to 15% or 25% of the blade tangential chord, C_t) had adjacent undamaged blades. As expected, the authors observed under-turning of the flow in the cut-out region, and—more interestingly—over-turning outside the cut-out region. Regions of over-turning were associated with streamwise vortices at the edges of the cut-out. The authors also found, perhaps surprisingly, that in the cut-out region, the losses were lower for the damaged blade than the undamaged blades. This was attributed to local thinning of the boundary layer (BL) due to the migration of BL fluid towards the notch edges. Overall, however, the blade with 25% cut-out depth (based on the tangential chord) suffered an increase in plane-averaged loss of 45%. The fact that this is the most relevant study to the current one (despite being incompressible rather than compressible, linear rather than annular, the article being a turbine blade, not a stator vane, and the component being uncooled as opposed to cooled) demonstrates the scarcity of literature in this area.

In a later—related—study in a transonic linear cascade ($\mathrm{Re} = 1 \times 10^6$, $\mathrm{M} = 1.2$, and $\mathrm{Tu} = 4\%$), Islam [2] performed midspan loss measurements two-fifths of an axial chord length downstream of the TE of uncooled turbine blades with simulated TE damage (semicircle cut-outs with depths equal to 10% and 20% of C_t). They found that midspan aerodynamic loss, as expected, would rise with increasing Mach number but, surprisingly, did not change significantly with the introduction of 10% or 20% cut-out depths. They also found that midspan exit flow angles were significantly altered, with an increase in the magnitude of under-turning with increasing exit Mach number and cut-out depth.

Wang et al. [3] numerically studied the impact of TE damage shape, location, and size (four levels of cut-out with depths between 9% and 37% of C_t) on the total pressure loss of a subsonic steam turbine nozzle ($\mathrm{M} = 0.5$). The following TE geometries were studied: three geometries with a single semicircle cut-out located at

---

[1] Corresponding author.

Contributed by the International Gas Turbine Institute (IGTI) of ASME for publication in the Journal of Turbomachinery. Manuscript received August 28, 2024; final manuscript received January 13, 2025; published online March 20, 2025. Assoc. Editor: Emil Goettlich.

different span locations (near the hub, midspan, and near the case); one geometry with two semicircle cut-outs at 25% and 75% span; and one geometry with an undamaged midspan region but significant burn-back near the case and hub. They found that loss increased with cut-out depth for all cut-out shapes. For semicircular cut-outs, the increase in loss was smallest when the cut-out was at the midspan and larger when it was at other span locations.

Bouchard et al. [4] investigated the performance of uncooled NGVs with TE distortion (rather than simulated burn-back) in a transonic annular cascade. The measurement plane was half an axial chord downstream of the TE. Their geometries included those with TE distortions towards the pressure surface (PS) and suction surface (SS) and with minor cracks at the TE. Total pressure traverse measurements were performed at four span locations (near-case; midspan; and two near-hub locations) for damaged and undamaged NGVs. They reported an increase in loss due to TE distortion of 38% at both hub and case; an increase of 72% in the midspan region; and an overall loss increase of 51%.

Meyer et al. [5] and Di Mare et al. [6] performed unsteady numerical simulations of the forced response of the HP turbine interacting with NGVs with triangular cut-out shapes. Both studies were full-stage whole-annulus with a single damaged vane into an otherwise undamaged stator row. Rajput [7] performed experiments on HP turbine forced response with upstream NGVs with different cut-out shapes (triangular, trapezoidal, rectangular) in the Rotating Cascade Tunnel Göttingen (RGG) at the German Aerospace Center (DLR) [8], a rotating annular cascade that can be operated at engine-matched conditions of Mach number, Reynolds number, and non-dimensional speed ($N/\sqrt{T}$). All of these studies had the following common findings: significant alteration of the flow field downstream of the damaged vane, with surprisingly little effect on the flow downstream of neighbouring vanes; counterrotating vortices downstream of the TE of vanes with simulated burn-back; and the alteration of the rotor blade loading when rotating past the damaged NGV as a result of the distortion of the NGV exit flow.

Michaud et al. [9] experimentally investigated the impact of in-service deterioration on the aerodynamic performance of heavily cooled transonic NGVs. The study used service-exposed vanes which exhibited: increased surface roughness; thermal barrier coating spallation; damaged film cooling holes; and mild TE burn-back. Experiments were performed in the Engine Component AeroThermal (ECAT) facility at the University of Oxford, an engine parts annular cascade operated at engine-matched conditions of Mach number, Reynolds number, and coolant-to-mainstream pressure ratio. A full area traverse was performed a quarter axial chord downstream of the TE using a combination of a single-hole probe (near endwalls) and a five-hole probe (roughly between 6% and 93% span region). A *rainbow-set* of new, mid-life, and end-of-life vanes was used to allow direct back-to-back measurements of the impact of deterioration. The authors found that deterioration caused an increase in overall mixed-out loss of up to 33% and flow under-turning of up to 6 deg. On parts with mild TE burn-back, vortices were formed at the edges of the burn-back region. In a complementary study, Michaud et al. [10] experimentally investigated the impact of in-service deterioration (the same parts) on the thermal performance of heavily cooled transonic NGVs. They performed ex situ (i.e., in the absence of the potential field developed by the vane) measurements of coolant capacity for each vane and in situ measurements of overall cooling effectiveness. The mean change in film coolant capacity and TE slot coolant capacity from new vanes was −2.20% and −4.87%, respectively, for the mid-life vanes and −5.77% and −16.80%, respectively, for the end-of-life vanes. They also found that changes in overall film cooling effectiveness were greatest on the PS and late SS; they measured changes in area-averaged overall cooling effectiveness of −1.83% and −10.41% on the PS of mid-life and end-of-life vanes, respectively.

In this paper, we perform a detailed parametric study of the impact of TE burn-back on performance, validating our methods using experimental data from the ECAT facility at the University of Oxford. This is an annular engine parts facility operated at engine-matched conditions of Mach number, Reynolds number, and coolant-to-mainstream pressure ratio. The parts used in this study were typical of a modern civil jet engine and were heavily film cooled. The data and resulting analysis are relevant to the whole-life modelling of turbine states.

2 Trailing Edge Damage Shapes

In this paper, we investigate four geometries with different levels of simulated TE damage, ranging from new parts to severely burnt-back parts. The geometries are illustrated in Fig. 1. We refer to these as Geometry 1 to Geometry 4. Illustrations of the midspan sections of these geometries are presented in Fig. 2, with the lines of the minimum geometric area highlighted. We parameterise the geometries using the depth of the damage feature, d, the width of the damage feature at the TE plane, w_1, and the width of the damage feature at the damage front, w_2. We compare the burn-back area, A_{BB}, to a reference area, A_{ref}, equal to the product of the tangential chord (C_{t}) and the span height (S). A summary of the values of these

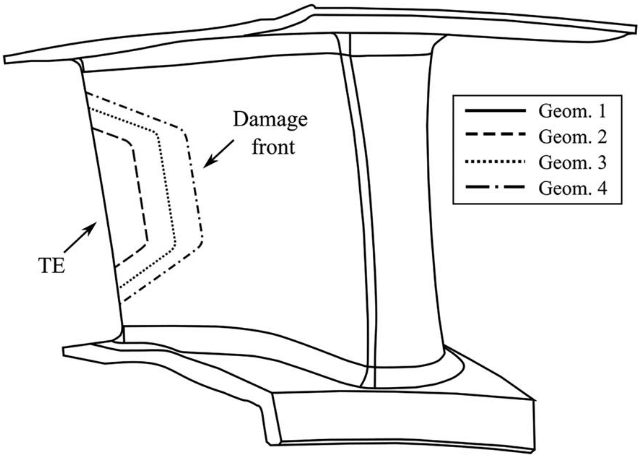

Fig. 1 Illustrations of Geometry 1–4 used in the simulations in this paper

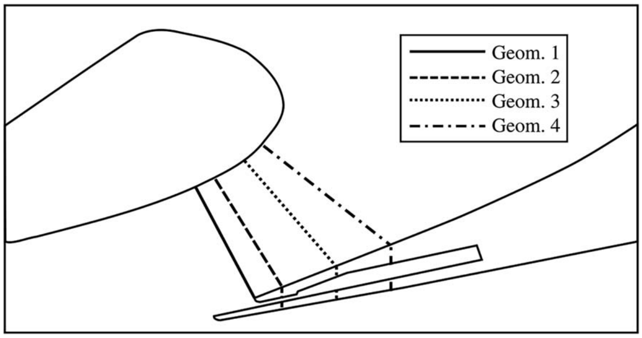

Fig. 2 Midspan-section illustrations of Geometry 1–4 with geometric minimum area lines highlighted

Table 1 Parametric descriptions of Geometry 1–4

	Geometry			
Non-dimensional damage shape parameters	1	2	3	4
Burn-back depth, d/C_{t} (%)	0	10.8	19.2	27.5
Burn-back width at TE, w_1/S (%)	0	42.5	54.6	66.8
Burn-back width at damage front, w_2/S (%)	0	29.8	33.3	36.8
Burn-back area, $A_{\mathrm{BB}}/A_{\mathrm{ref}}$ (%)	0	3.9	8.4	14.2

characterisation parameters, for each of the four geometries, is given in Table 1.

The form and size of these damaged shapes are based on a statistical analysis of hundreds of real-engine parts subject to TE burn-back. The data showed that TE burn-back regions were often approximately trapezoidal in form and that the mean centre of the damage front was approximately at midspan. Similar analysis and conclusions can be found in Meyer et al. [5].

3 Experimental Method

Area traverse measurements for Geometry 1–4 were performed using the ECAT facility at the University of Oxford. The ECAT facility is a high technology-readiness-level blowdown facility normally configured with an annular cascade of real-engine NGV parts. It has the capability for very accurate metal effectiveness, capacity, and aerodynamic loss measurements at non-dimensionally matched engine conditions (M, Re, and p_{0c}/p_{01}). The facility can be operated with and without a combustor simulator. A schematic of the ECAT facility working section (configured without the combustor simulator) is shown in Fig. 3.

Pressurised air is supplied to the facility from large tanks which feed the mainstream and coolant flows. For the current experiments, the ECAT facility was operated in regulated mode, such that operating conditions are maintained constant for over 60 s during a run. This allows aerodynamic traverse measurements at a single operating point. The operating conditions used in this study are summarised in Table 2.

The mainstream flow inlet total pressure and total temperature were measured using four pitot probe rakes and four thermocouple rakes three axial chord lengths upstream of the vane leading edge. Exit static pressure was evaluated using 84 surface static tappings distributed over 6 vanes (out of 40), with tappings located a third of an axial chord length downstream of the TE midspan location. Area traverse measurements were performed at a single axial plane located a quarter axial chord length downstream of the vane TE. The inlet measurement plane, static pressure tapping locations, and the traverse measurement plane are marked in Fig. 3.

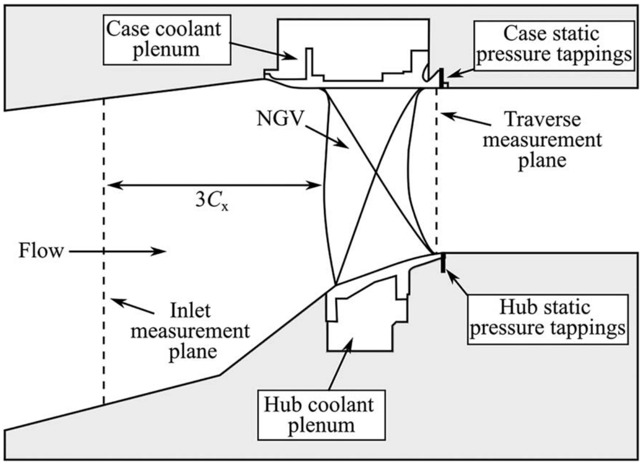

Fig. 3 Schematic of ECAT facility working section (without combustor simulator), adapted from [11]

Table 2 ECAT facility operating conditions used for this study

Variable	Value
Mainstream inlet total pressure, p_{01} (bar)	2.0
Mainstream inlet total temperature, T_{01} (K)	287
Coolant inlet total temperature, T_{0c} (K)	287
Vane pressure ratio, p_{exit}/p_{01} (–)	0.534
Coolant-to-mainstream pressure ratio, p_{0c}/p_{01} (–)	1.026
Reynolds number based on the tangential chord, Re (–)	1.6×10^6
Exit Mach number, M_{exit} (–)	0.98

For the area traverse measurements, a radial-circumferential traverse mechanism was used. In the 5.8–93.2% span region, a five-hole probe (with tip diameter of 2.8 mm) calibrated over a wide range of Mach numbers ($0.3 \leq M \leq 1.4$) and incidence angles (±40 deg in both pitch and yaw directions) was used to measure the total and static pressure, flow angles, and Mach number. In the near-wall regions (1.7–5.8% span and 93.2–97.5% span), a pitot probe (with tip diameter 0.8 mm) was used to measure the total pressure. Overall, 96% of the vane span (1.7–97.5%) was surveyed. Probes were aligned with the mean metal angle to minimise the incidence angle. Traverse measurements covered 4.5 vane passages. Further details of the facility can be found in the following references: Kirollos et al. [11] present details of the facility architecture and operation; Messenger and Povey [12] and Michaud et al. [13] provide details of high-temperature operation and independent adjustment of Re and M, respectively; the traverse system and traverse data reduction are described in detail in Burdett et al. [14] including detailed uncertainty analysis; a comprehensive discussion of averaging methods in the context of this data is given by Burdett and Povey [15].

4 Numerical Method

CFD simulations were performed using the ANSYS-CFX solver with steady Reynolds-averaged Navier–Stokes (RANS) settings and second-order discretization for the advection and turbulence terms. Simulations were performed with the baseline k–ω explicit algebraic Reynolds stress model (BSL-EARSM). Amend and Povey [16] demonstrated better agreement with similar experimental data for BSL-EARSM than other commonly used turbulence models (e.g., k–ω shear stress transport (SST) and Spalart–Allmaras turbulence models). The computational domain (Geometry 1) is shown in Fig. 4: it includes a vane pair with two complete passages.

An unstructured octree-based mesh was generated for each domain (Geometry 1–4) using BOXERmesh. A midspan view of the mesh for Geometry 1 is shown in Fig. 5. The NGV surface and the internal walls of the TE slot were refined with 30 and 15 inflation layers, respectively, with an initial step size of 3 μm to achieve y^+ values less than two on most of the wetted surfaces. The hub and case endwalls were refined with 25 inflation layers with an initial step size of 6 μm to achieve y^+ values less than five. The mesh was refined in the wake, near the TE, in the throat area, and around the NGV surface. Wake refinement was optimised by exporting an iso-volume defined by a total pressure value from an initial uncooled RANS solution. A mesh sensitivity study was performed to ensure that: all important solution parameters were independent of the mesh and

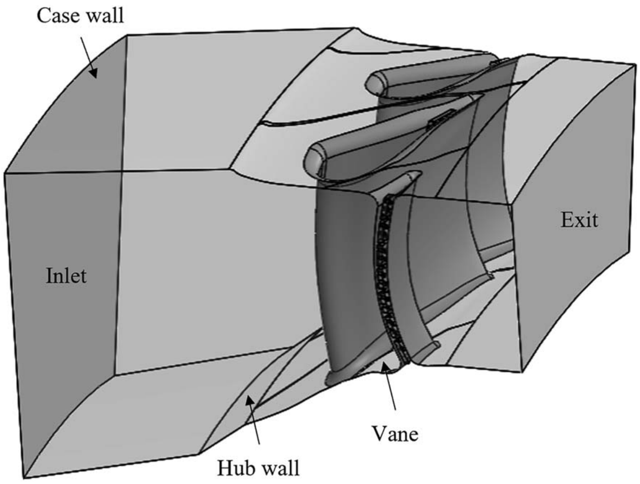

Fig. 4 Computational domain (Geometry 1) for simulations

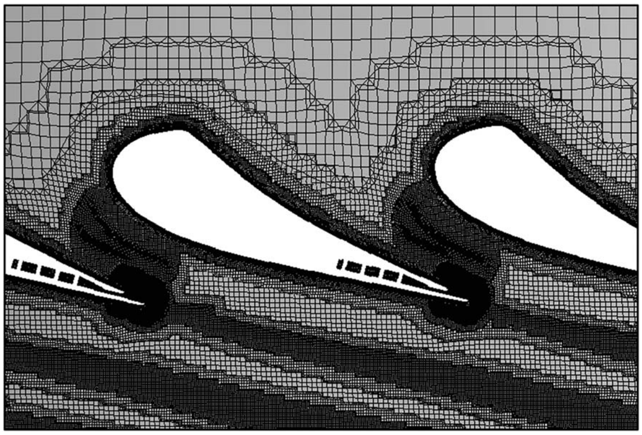

Fig. 5 Midspan view of the mesh (Geometry 1)

the viscous sublayer was captured within the near-wall inflation layers. The final meshes each had ~60 million cells.

Domain boundary conditions matched those of the experiment (Table 2). At the inlet, radial profiles of total pressure, total temperature, turbulence length scale, and turbulence intensity were imposed; these were taken from experimental measurements at the inlet measurement plane (see Amend et al. [17] for further details of the upstream traverse mechanism and sample radial profiles). At the exit, an area-averaged static pressure was imposed, with an unconstrained radial profile to satisfy radial equilibrium in the exit flow [18]. Particular care was taken to evaluate the vane exit static pressure in the CFD solutions at identical monitor points to experimental measurement locations: the exit static pressure boundary condition in the CFD was then adjusted to exactly match the experimental value used for traverse measurements. Solid walls were set as adiabatic boundaries. Periodic boundaries were used in the circumferential direction. Film cooing was modelled using area patches with hole size and geometry, hole location, mass flowrate, and direction vectors specified on a per-hole basis. The TE slot was explicitly modelled including features such as ribs and pedestals. Within the TE slot for this particular design, chordwise ribs divide the plenum into fourteen ducts. The mass flowrate at each duct inlet was independently specified.

Coolant mass flowrates for individual film holes and the TE slot were determined using an in-house low-order (one-dimensional) internal flow solver and then scaled to match the coolant-to-mainstream mass flow ratio measured in the experiments. This low-order code uses empirical correlations for friction factors and discharge coefficients (from Ref. [19]) in a nodal representation of the internal cooling system. Coolant inlet total pressure and total temperature and the film cooling hole exit static pressures are imposed as boundary conditions. The external static pressure distribution was obtained from an initial uncooled CFD prediction.

5 Experimental and Numerical Results

In this section, we consider the capability of the CFD method by detailed comparison of experimental and CFD results, and the impact of simulated TE burn-back on aerodynamic performance. The latter is progressed by considering the impact of increasing—simulated—burn-back on: local kinetic energy (KE) loss coefficient distributions; local axial vorticity distributions; radial distributions of circumferentially averaged KE loss coefficient; radial distributions of circumferentially averaged exit flow angle; BL profiles and loss; vane loading distributions and coolant loss; and overall aerodynamic performance.

5.1 Distributions of Local Kinetic Energy Loss Coefficient.

As one metric for performance, we compare experimental measurements and CFD predictions of total pressure loss as measured by the local kinetic energy loss coefficient, ζ' (for discussion of loss metrics, see Ref. [15]), defined by

$$\zeta'(r,\theta) = 1 - \frac{1-(p_2(r,\theta)/p_{02}(r,\theta))^{(\gamma-1)/\gamma}}{1-(p_2(r,\theta)/p_{01})^{(\gamma-1)/\gamma}} \qquad (1)$$

where $p_2(r,\theta)$ and $p_{02}(r,\theta)$ are the local static and total pressures in the plane of interest, p_{01} is the inlet total pressure (assumed uniform), and γ is the ratio of specific heats ($\gamma = 1.4$ for air). Distributions of $\zeta'(r,\theta)$ in the downstream traverse measurement plane (see Fig. 3) for Geometry 1–4 are shown in Fig. 6. Both experiment and CFD-predicted distributions of $\zeta'(r,\theta)$ have been normalised by the experimentally measured mixed-out loss coefficient for Geometry 1, ζ''''_{ref} (defined later).

Consider first the experimentally measured $\zeta'(r,\theta)$ distribution for Geometry 1. The curved wake results from compound lean in the aft-chord region of the vane. Along the line of the wake, there are a number of local maxima and minima, due to the presence of chordwise ribs within the TE slot. Loss along the line of the wake is greater at the endwalls than at the midspan region, as a result of the endwall BL fluid migration towards the vane-endwall SS corner. Near the casing and hub regions (~85% and ~10% span respectively), there are regions of higher loss associated with passage vortices. We discuss these in a later section. The vane design (including compound lean) means that the distance between the traverse plane and the *local* TE is smaller at the hub and case than at the midspan. This, in part, accounts for the greater degree of mixing at midspan than at case and hub.

Consider now the CFD predictions of the local $\zeta'(r,\theta)$ distributions for Geometry 1. We see that the prediction captures the wake shape and secondary loss core locations well, but the peak value of ζ' in the wake is overpredicted due to undermixing (with respect to the experiment) in the CFD solution. This is analysed in detail in Refs. [17,20].

Now consider the impact of TE burn-back. Considering the evolution of the loss coefficient distribution in both experiment (left column) and CFD (right column), with increasing TE burn-back, we see the following effects:

1. Significant alteration of the shape of the wake, with an increasing counter-clockwise (CCW) VFD *lag* of the wake in the burn-back region as the burn-back increases. This results from under-turning in the burn-back region due to TE material removal. Perhaps more interestingly, outside the burn-back region (near hub and case), there is increasing clockwise (CW) VFD migration with increasing burn-back, indicating over-turning of the flow. We will see later that this results from the formation of a vortex pair at the edges of the TE burn-back feature.
2. Increased intensity of hub loss core, with CCW VFD circumferential migration, and radial migration away from the wall.
3. Increased intensity of the casing loss core, with CW VFD migration, and radial migration away from the wall.
4. Development of significant new loss cores at the edges of the burn-back region (at approximately 25% and 75% span) which strengthen with increasing burn-back. We later associate these loss cores with two distinct counterrotating vortices.
5. Radial migration of the wake fluid within the burn-back region from the burn-back corners (at approximately 25% and 75% span) towards the midspan (50% span) resulting in lower loss at the burn-back corners and higher midspan loss. The effect is to collect the loss at midspan.
6. Broadening of the wake outside the burn-back region, and thinning of the wake within the burn-back region. We quantify this in a later section.

For all four comparisons (Geometry 1–4), CFD predicted the wake shape and locations of secondary loss core locations well but overpredicted the peak value of ζ' in the wake. Overall, we take the CFD method to perform adequately for the purpose of

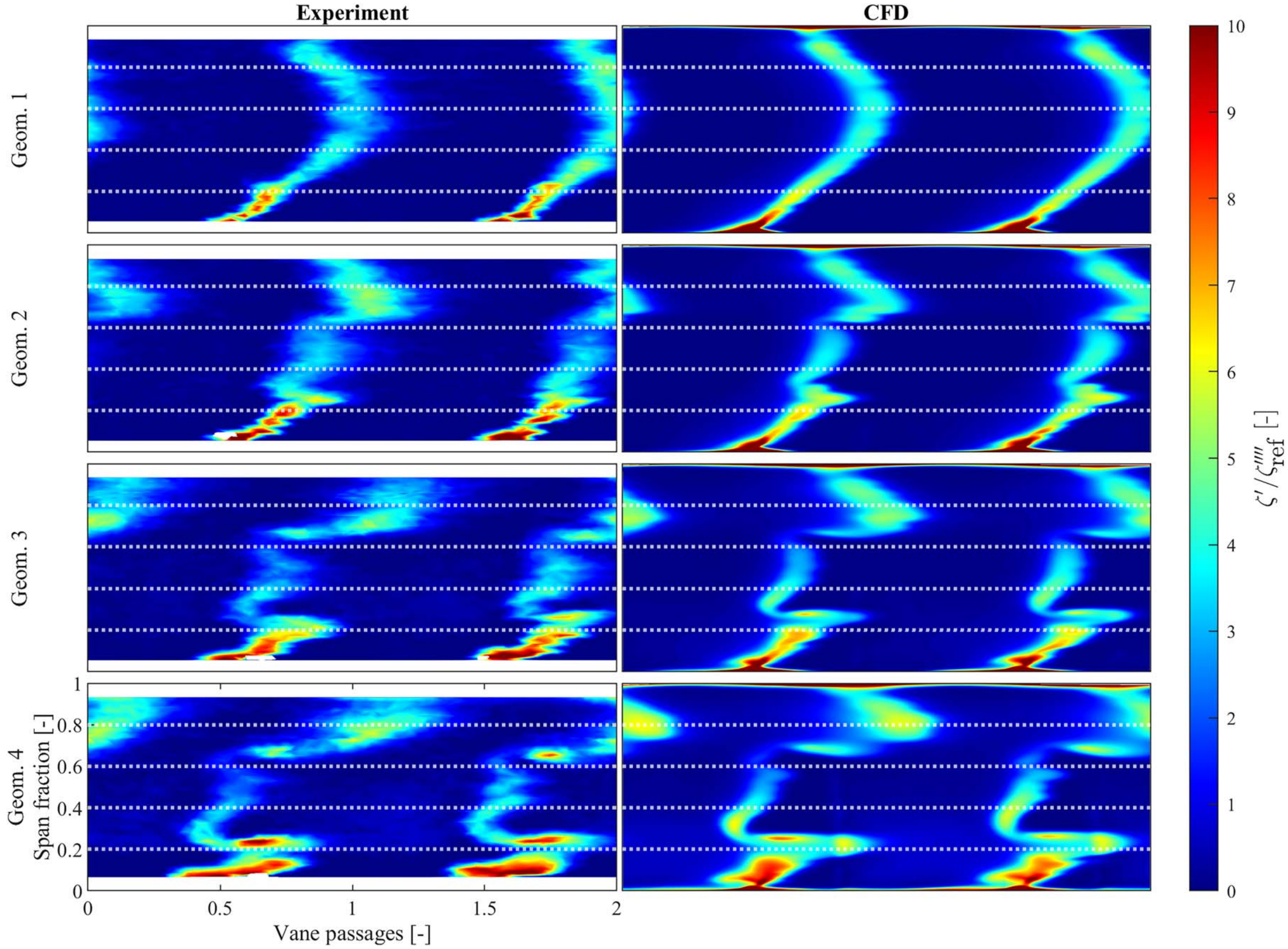

Fig. 6 Distributions of normalised local KE loss coefficient, $\zeta'/\zeta''''_{\text{ref}}$, for Geometry 1–4 for experiment and CFD predictions. Data are viewed from downstream (VFD); the principal exit flow direction is CW VFD

predicting general trends of downstream loss (both magnitude and distribution) while noting the tendency to be undermixed with respect to the experiment.

5.2 Axial Vorticity Distributions. We will now investigate the impact of TE burn-back on the downstream secondary flow by interrogation of CFD simulations. We use the axial vorticity, ω_x, parameter in Cartesian coordinates

$$\omega_x = \left(\frac{\partial v_z}{\partial y} - \frac{\partial v_y}{\partial z}\right) \tag{2}$$

where v_y and v_z are the components of the velocity vector normal to the axial direction in the measurement plane.

We first consider the secondary flow structures for Geometry 1. Local distributions of axial vorticity for uncooled RANS and cooled RANS simulations are shown in Fig. 7. The SS is to the left of the wake, and the PS is to the right. The axial vorticity is normalised by the maximum freestream axial vorticity value of the cooled RANS solution. Here, positive axial vorticity indicates CCW rotation when VFD, and negative axial vorticity indicates CW rotation when VFD.

Consider first the uncooled solution. We mark in the figure: the PS legs of the horseshoe vortex or passage vortex; the SS legs of the horseshoe vortex, or counter vortex; and the corner separation vortex. Here, we use the terminology of Ref. [21], which is in widespread use. These appear on the SS of the vane. The cooled solution is relatively similar to the uncooled solution and shows many of the

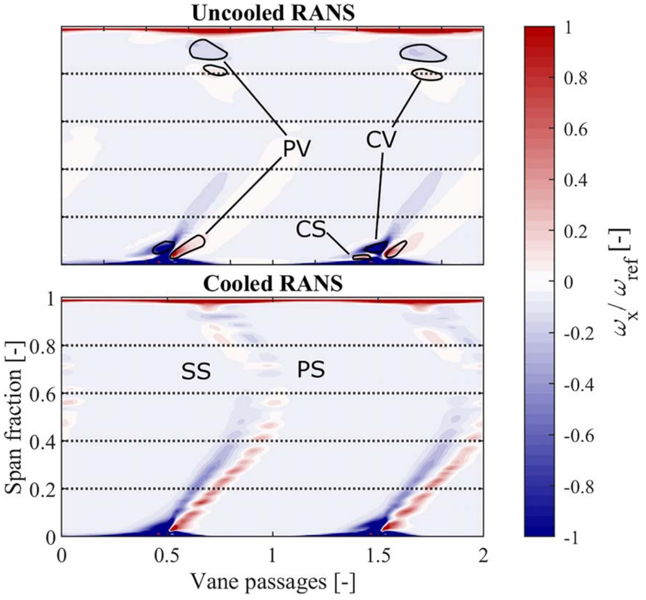

Fig. 7 CFD-predicted axial vorticity distributions, ω_x, for uncooled RANS and cooled RANS. Data are VFD; the exit flow direction clockwise VFD

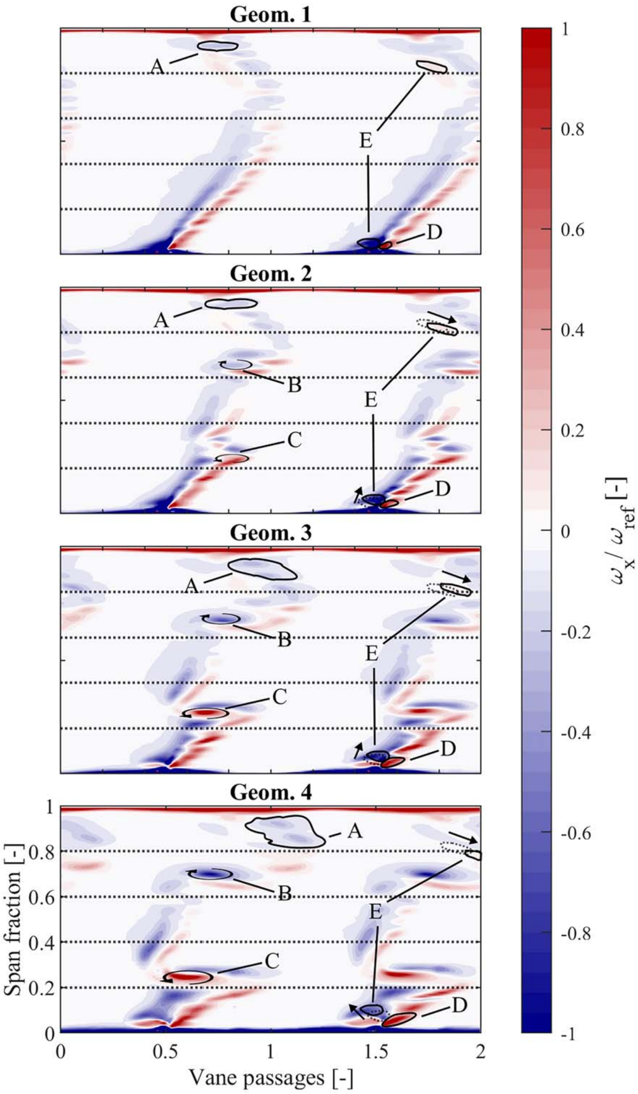

Fig. 8 Axial vorticity distributions, ω_x, from CFD prediction for Geometry 1–4. Data are VFD; the exit flow direction CW VFD

same weak vortex structures. We note additional small vorticity peaks along the line of the wake (apparently associated with individual coolant jets, based on the count), and an enhanced line of mildly negative vorticity between 0% and 40% span on the SS of the wake, with an accompanying line of mildly positive (with respect to the background level) vorticity on the PS of the wake.

We now consider the CFD predictions for Geometry 1–4. Local distributions of axial vorticity for cooled RANS simulations are shown in Fig. 8. With burn-back we see:

(1) Development of a pair of vortices at the edges of the burn-back region marked B and C in plots for Geometry 2–4. These are illustrated in Fig. 9. We discuss them later in this section. The two vortices are counterrotating relative to each other: the casing vortex has a clockwise rotation VFD and the hub vortex has a counter-clockwise rotation VFD. The intensity of these vortices increases with increasing burn-back: peak values of normalised axial vorticity for the burn-back vortex closest to the hub were 0.91, 1.37, and 1.56 for Geometry 2, 3, and 4, respectively.

(2) Increasing displacement of the wake in the cut-back region with respect to the near-hub and near-case wake; this has already been commented on in the context of Fig. 6.

(3) Migration, distortion, and growth of the case passage vortex (marked A in Fig. 8), as a result of the interaction between the burn-back vortices and other secondary flow. This feature is tracked and marked A in plots for Geometry 2–4, and we can see it combined with other features.

(4) Migration and distortion of the counter vortices (marked E in Fig. 8; dotted regions show position in previous build).

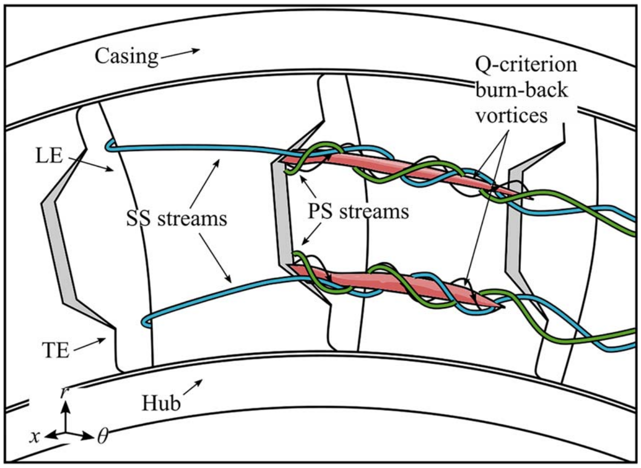

Fig. 9 Schematic representation of burn-back vortices for Geometry 4, visualised by Q-criterion

In summary, with TE burn-back, a pair of counterrotating vortices forms at the burn-back edges. These strengthen with increasing burn-back and result in two additional loss cores. The action of these additional secondary flows appears to enhance existing secondary flows.

We now consider the burn-back vortices in more detail. A schematic representation of these vortices for Geometry 4 is shown in Fig. 9. The schematic is based on the Q-criterion in the CFD solution. These counterrotating vortices form due to significantly mismatched whirl and velocity at the edges of the burn-back region. In the burn-back region, both the whirl and velocity are reduced compared to the neighbouring (higher and lower span) regions. This results in a shearing flow at the burn-back edges, that mixes out into a vortex. The burn-back vortices are further visualised by PS and SS streamlines as shown in Fig. 9.

5.3 Radial Distributions of Circumferentially Mass-Flux-Averaged Kinetic Energy Loss Coefficient.

We now consider the experimentally measured and CFD-predicted spanwise variation of the circumferentially averaged loss coefficient, $\zeta''(r)$, defined by

$$\zeta''(r) = 1 - \frac{1 - \left(\bar{p}_2(r)/\bar{p}_{02}(r)\right)^{(\gamma-1)/\gamma}}{1 - \left(\bar{p}_2(r)/p_{01}\right)^{(\gamma-1)/\gamma}} \tag{3}$$

where $\bar{p}_2(r)$ is the circumferentially area-averaged static pressure at a particular span height, r, and $\bar{p}_{02}(r)$ is the circumferentially mass-flux-averaged total pressure.

Radial distributions of the loss parameter $\zeta''(r)$ are shown in Fig. 10 for Geometry 1–4 for both experiment and CFD predictions. Experimental data are recorded in the 6–93% span range (limitations due to the size of the five-hole probe). Consider first the Geometry 1 data (solid line). In both, the experimental data and CFD prediction, the loss coefficient is relatively uniform between 20% and 80% span. In this *profile-loss region* (loosely defined), the loss is dominated by the BL development and TE flow, both of which depend on the surface Mach distribution and TE Mach number. The flow in this region is relatively unaffected by secondary flows. The mean values of $\zeta''/\zeta''''_{\mathrm{ref}}(r)$ in this span range were 0.800 for the experiment and 0.764 for the CFD, a good match. Small radial fluctuations are attributed to the intermittent chordwise slot within the TE (discussion in the context of Fig. 7); these can be seen in both the experiment and CFD. Outside of the profile-loss region, the loss increases rapidly in the approach to the endwalls

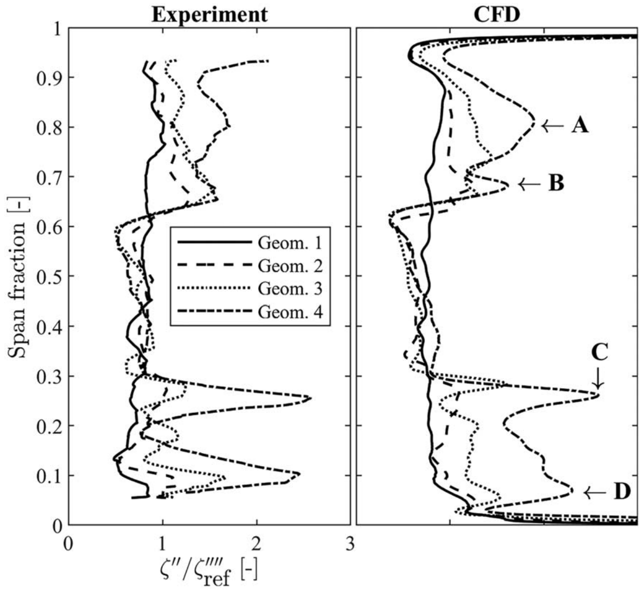

Fig. 10 Radial distributions of circumferentially mass-flux-averaged kinetic energy loss coefficient, $\zeta''(r)$, for Geometry 1–4 for experiment and CFD predictions

(accumulation of low-momentum fluid in the endwall region). Some of this endwall fluid is migrated away from the wall into secondary loss cores: see, for example, at 8% span in the experiment and 4% span in the CFD prediction.

Considering now the rest of the experimentally measured data and CFD simulations, the effect of burn-back is as follows:

(1) Development of two new loss cores (marked B and C in Fig. 10) due to vortex formation at the edges of the burn-back region (see the previous section). These move with the changing burn-back front (see Fig. 1) and increase in magnitude with increasing burn-back (by 23% and 157% experimentally for vortices B and C, respectively, between Geometry 2 and Geometry 4).

(2) Strengthening of the hub and casing loss cores with increasing burn-back (marked A and D in Figs. 8 and 10) and due to the interaction with the newly formed vortices at the edges of the burn-back region. The magnitude of the peak loss values increases between Geometry 1 and Geometry 4 by 86% at A and 189% at D.

(3) The location of the hub and casing loss core peaks (at A and D) also move towards mid-passage with increasing burn-back (from 87% to 80% span for loss core A and from 8% to 10% span for loss core D). This is due to the inward migration of the SS flow towards the low-pressure burn-back region. The effect is shown by the surface streamline patterns of Fig. 11.

(4) Disproportionate increase in hub region (5–25% span) loss arising from an increase in Mach number in this already high-M region (see section on vane loading distributions).

(5) In the burn-back region (32–58% span for Geometry 4) the experimentally measured mass-flux-averaged loss decreased slightly (by 8%) between Geometry 1 and Geometry 4. This is surprising because, despite shorter wetted surface length with burn-back, there is an increase in boundary layer loss (see later discussion). The result is explained by the fact that fluid in the wake is redistributed away from the midspan in the flow immediately downstream of the TE, as it is entrained into the burn-back vortices. Sjolander et al. [1] and Islam [2] report a similar result, also attributing it to wake fluid being swept into the burn-back vortices.

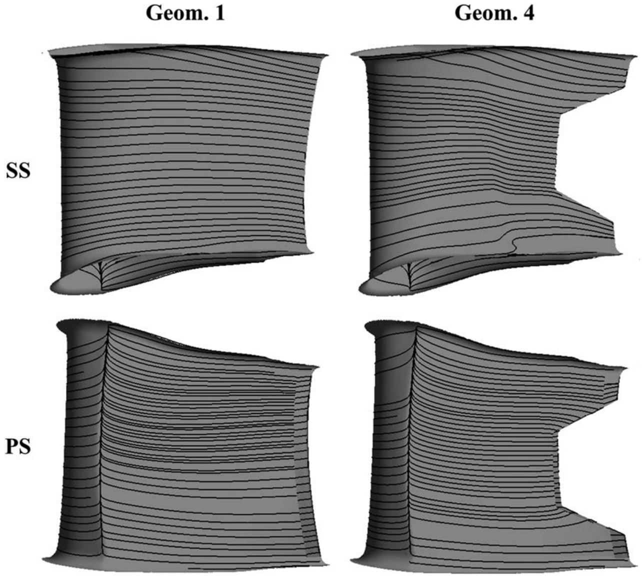

Fig. 11 CFD-predicted vane surface streamlines for Geometry 1 and Geometry 4 on the SS and PS

Table 3 Percentage changes (from Geometry 1) in mass-flux-averaged loss coefficient for case, profile, and hub regions

Geometry	$\Delta\zeta''_{\mathrm{CASE}}$ (%)	$\Delta\zeta''_{\mathrm{PROFILE}}$ (%)	$\Delta\zeta''_{\mathrm{HUB}}$ (%)
	Experiment		
1 → 2	+7	+16	+27
1 → 3	+26	+18	+80
1 → 4	+72	+35	+141
	CFD		
1 → 2	+6	+5	+13
1 → 3	+25	+12	+50
1 → 4	+73	+41	+135

We also see that for all four simulations (Geometry 1–4), CFD predicted the radial profiles of loss well, with the radial locations and magnitudes of loss peaks determined accurately. This lends confidence to the CFD method used in this study.

We now calculate the change in mass-flux-averaged loss coefficient from the Geometry 1 case, for three regions of the flow: hub, 0–20% span; profile, 20–80% span; and case, 80–100% span. These data are summarised in Table 3.

We see that the loss increased in all three regions for all three comparison points (1 → 2, 1 → 3, and 1 → 4) for both the experimental results and CFD. The comparison of absolute changes measured experimentally and predicted by CFD was good; the average of ratios of individual terms (the nine ratios formed from data of Table 3) was 0.783 (c.f. unity for perfect prediction) with a standard deviation of 0.263. The loss increase was greatest at the hub (same result as Bouchard et al. [4]), middling at the casing, and smallest in the profile region.

5.4 Radial Distributions of Circumferentially Mass-Flux-Averaged Exit Flow Angle.

We consider now the experimentally measured and CFD-predicted spanwise variation of the circumferentially mass-flux-averaged exit flow angle, $\beta'(r)$, for Geometry 1–4. Spanwise profiles for both experimental measurements and CFD predictions are shown in Fig. 12.

Looking first at Geometry 1 (solid lines in Fig. 12) data, we see that between 20% and 80% span, the general trend in both experiment and CFD is an almost-linear increase in flow angle from hub to case. This broadly follows the TE PS metal angle (with expected

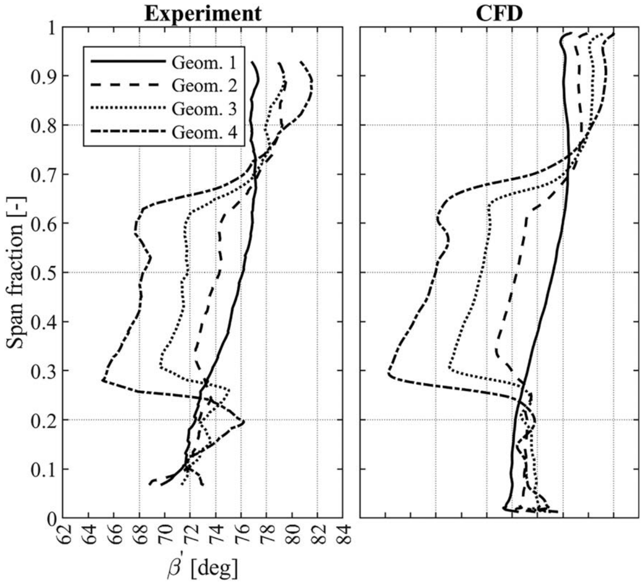

Fig. 12 Radial distributions of circumferentially mass-flux-averaged exit flow angle, $\beta'(r)$, for Geometry 1–4 for experiment and CFD predictions

deviation). In this region, the mass flow-averaged whirl angle was 75.6 deg in the experiment and 76.9 deg in the CFD prediction, a 1.3-deg difference. The probe bias error was ±0.8 deg quoted to 95% confidence (for uncertainty analysis, see Refs. [14,17]). We also note small geometric differences between the experiment and CFD computer aided design (CAD); the latter was the nominal design geometry and did not include surface roughness features, nor specific assessment of batch nonconformity.

Now consider the impact of TE burn-back. This leads to reduced turning in the burn-back region and—interestingly—increased turning outside the burn-back region. The measured peak values of *under*-turning (from the Geometry 1 reference) at 50% span were 1.9, 4.4, and 7.8 deg for Geometry 2, 3, and 4, respectively. Corresponding values for *over*-turning at an 85% span were 1.9, 2.4, and 4.5, respectively.

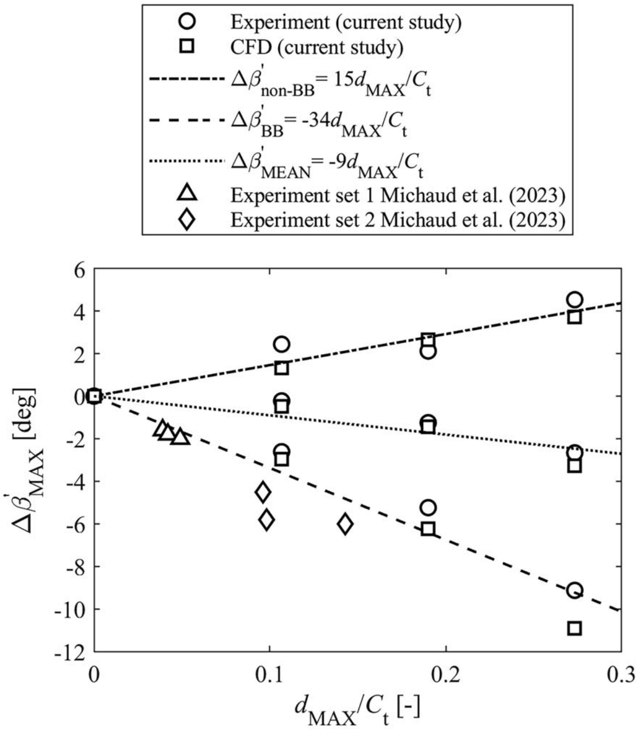

Fig. 13 Maximum flow angle deviation (from nominal) with burn-back damage depth

The under-turning in the burn-back region can be partially attributed to metal angle reduction: the geometric changes between Geometry 1 and Geometry 2, 3, and 4 were 0.93, 1.81, and 2.69 deg, respectively, accounting for on average—42% of the measured under-turning at midspan. The remaining part of the under-turning effect is attributed to insufficient turning length with the truncated vane (effective increase in pitch-to-chord ratio on account of reduced chord length), leading to a significant deviation angle at exit.

The (milder) over-turning outside the burn-back region (an effect predominantly at the casing) is explained by an increase in peak SS Mach number at all span locations, causing a greater cross-passage pressure gradient. In the spanwise locations outside the burn-back region, for which the vane surface length is unaffected, this enhances turning. For the Geometry 4 configuration, the experimental peak whirl angle (81.5 deg at 86% span) exceeds the local metal angle by 7.3 deg.

The CFD was in very good agreement with the experimental data for all four builds but with a tendency to over-predict the degree of under-turning (by 1.2 deg on average) and underpredict the degree of over-turning (by 0.8 deg on average).

We use these data to establish simple (rule of thumb) linear relationships between the maximum TE burn-back damage depth, $d_{\mathrm{MAX}}/C_{\mathrm{t}}$; the maximum flow angle deviation (from nominal flow angle) in the burn-back region, $\Delta\beta'_{\mathrm{BB}}$; the maximum flow angle deviation outside the burn-back region, $\Delta\beta'_{\text{non-BB}}$; and the mean flow angle deviation, $\Delta\beta'_{\mathrm{MEAN}}$. The experimental and CFD data points are shown in Fig. 13. The forms $\Delta\beta'_{\mathrm{BB}} = -34 d_{\mathrm{MAX}}/C_{\mathrm{t}}$, $\Delta\beta'_{\text{non-BB}} = 15 d_{\mathrm{MAX}}/C_{\mathrm{t}}$, and $\Delta\beta'_{\mathrm{MEAN}} = -9 d_{\mathrm{MAX}}/C_{\mathrm{t}}$ were good fits to the data (R^2 values of 0.957, 0.911, and 0.840, respectively). We also compare our data points with the study of Michaud et al. [9] (data plotted in Fig. 13, but not used for regression) conducted in the same research group a few years ago. The study of Ref. [9] used a similar working section, followed similar procedures, and used vanes from the same engine family. An important difference is that the current study uses artificial (idealised) burn-back geometry whereas Ref. [9] used in-service deteriorated parts. Despite these differences, there is good agreement between the two datasets.

In summary, TE burn-back has a significant impact on the downstream vane exit flow angle distribution, partly as the direct result of TE material removal, but also due to the impact of new secondary flow vortices and vane reloading in response to the material removal. This has implications for stage performance, and also rotor design, if acceptable stage performance is required even for deteriorated nozzle parts.

5.5 Vane Loading Distributions.

We now investigate the impact of increasing burn-back on the vane loading distributions. CFD-predicted vane surface isentropic Mach number distributions at 15%, 50%, and 85% span fraction for Geometry 1–4 are shown in Fig. 14. The axial distance, x, is normalised with respect to the axial chord of Geometry 1, $C_{x,1}$. Note that in each CFD case, the same inlet total pressure profiles were used for all simulations, but the exit static pressure boundary condition (see numerical methods for more detail) was varied to exactly match the mean experimental exit pressure based on identical monitor points. The measured (and matched-CFD) row pressure ratios for our data varied between 0.534 and 0.539, resulting in an exit Mach number range of $0.983 < \mathrm{M}_{\mathrm{exit}} < 0.991$. We will see that this is a small variation compared with that induced by the change in geometry.

Consider first the baseline geometry (Geometry 1). The surface isentropic Mach number distributions are typical of a moderately forward-loaded vane, with peak Mach number between 60% and

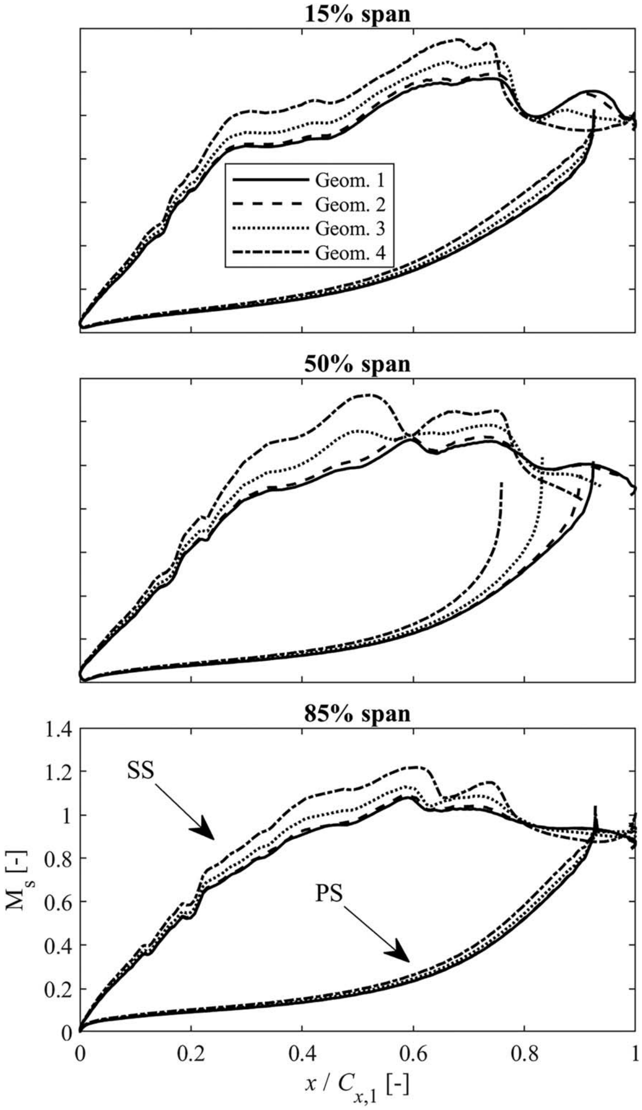

Fig. 14 CFD-predicted NGV surface isentropic Mach number distributions at 15%, 50%, and 85% span for Geometry 1–4

80% axial chord. Peak Mach numbers at 15%, 50%, and 85% span were approximately 1.15, 1.12, and 1.08. The uncovered turning region (see Fig. 5), $0.6 < x/C_{x,1} < 1.0$, has a complex interaction with the neighbouring passage flow, with transonic peaks beyond the controlling region around the point of minimum physical area. On the PS, there is a well-behaved acceleration at all span locations.

Now consider the cases with TE burn-back. With increasing burn-back, we see the following effects:

1. A significant increase in mid-chord ($0.3 < x/C_{x,1} < 0.7$) SS isentropic Mach number at all span locations, leading to both increased peak loading and increased forward loading. Peak SS M increased to 1.35, 1.32, and 1.20 at 15%, 50%, and 85% span. At 50% span, the location of peak M moves forward, from approximately $x/C_{x,1} = 0.6$ (Geometry 1) to approximately $x/C_{x,1} = 0.5$ (Geometry 4).
2. A decrease in late ($x/C_{x,1} > 0.8$) SS Mach number which—in combination with the previous effect—increases the adverse pressure gradient on the late SS leading to thickening of the SS BL (see next section). At the 15% and 50% span sections, with increasing cut-back the gradient in adverse pressure increases sharply (suggested presence of shock).
3. A mild increase in late ($x/C_{x,1} > 0.6$) PS Mach number. Note that in the cut-back region (50% span in Fig. 14), there is also a more significant change in the position of the PS cut-back location than the SS cut-back location, because of the geometry of the cut-back (see Fig. 2).

TE burn-back has a significant effect on the vane aerodynamics. We now consider the impact of aerodynamic changes on the boundary layer profiles and loss.

5.6 Boundary Layer Profiles and Loss. We now consider the effect of TE burn-back on the BL profiles. For our design, BL loss accounts for approximately 30% of total loss. The CFD-predicted normalised PS and SS BL profiles at 5%, 25%, 50%, 75%, and 95% span at the TE for Geometry 1–4 are shown in Fig. 15. The surface-normal distance, y, has been normalised by the minimum geometric throat width of the Geometry 1 vane at 50% span, y_{t1}. The local velocity, $u(y)$, has been normalised by particular local freestream velocities, U_{PS} and U_{SS}, determined as follows: for the PS, the freestream velocity at $y/y_{t1} = 0.05$; for the SS, the freestream velocity at $y/y_{t1} = 0.20$. These values are just outside the thickest BLs on each surface (noting that in the case of the SS, there is ambiguity because the scales of the BL velocity gradient and cross-passage velocity gradient are more similar). Normalised boundary layer displacement thickness, δ^*/y_{t1}, and momentum thicknesses, θ/y_{t1}, are also computed as a function of span for all builds.

Consider first the BL profiles for the baseline (Geometry 1) vane. This is shown by solid lines in Fig. 15, where the colours identify the PS and SS BL profiles, respectively. The SS BL is approximately 11 times thicker than the PS BL: the normalised displacement thicknesses (δ^*/y_{t1}) for the SS and PS BLs were 0.022 and 0.002, respectively. The corresponding normalised momentum thicknesses (θ/y_{t1}) were 0.014 and 0.001 for the SS and PS BLs, respectively. That is, the mean SS momentum thickness is 13 times larger than the PS momentum thickness and the loss is dominated by this surface. These results are in line with other studies, e.g., from Mee et al. [22], who measured a momentum thickness

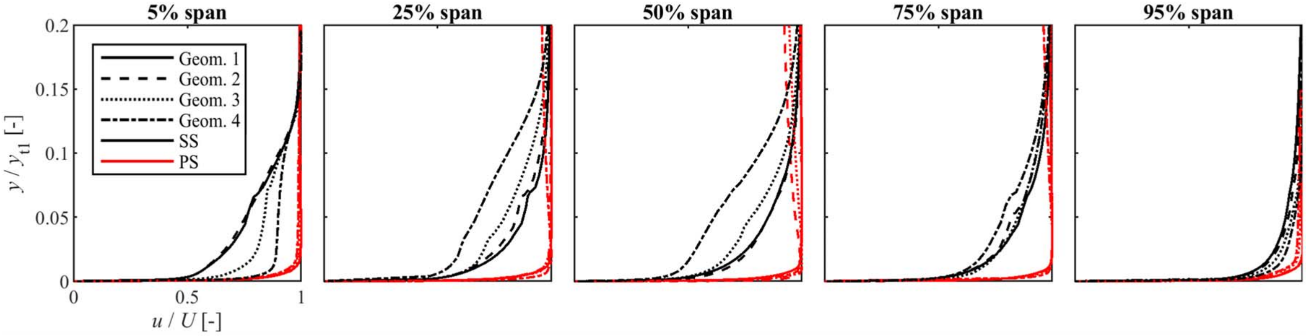

Fig. 15 CFD-predicted normalised PS and SS BL profiles for Geometry 1–4 at five different span locations

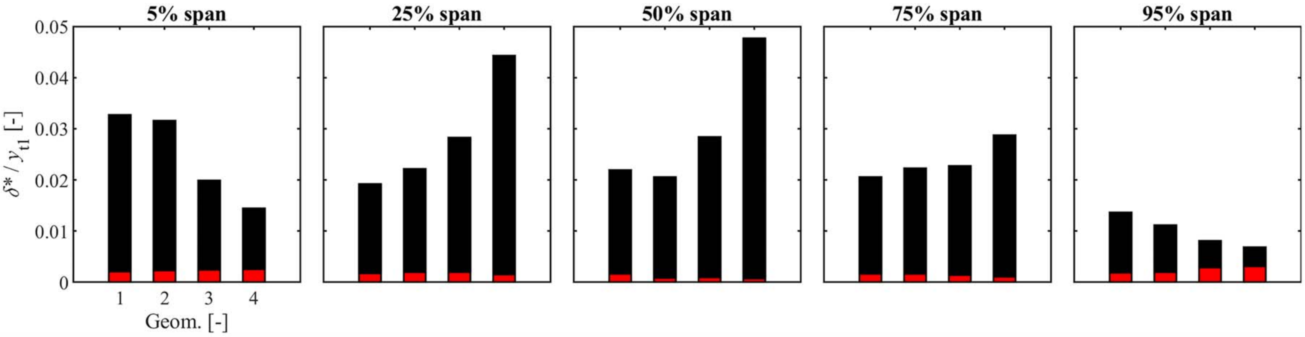

Fig. 16 CFD-predicted normalised PS and SS displacement thicknesses for Geometry 1–4 at five different span locations

at the TE of a transonic turbine blade that was nine times larger on the SS than the PS. The BL is thicker on the SS as this fluid experiences an adverse pressure gradient near the TE, whereas the PS fluid experiences a favourable pressure gradient.

We now consider the impact of TE burn-back on the BL profiles. We see the following effects:

(1) In the burn-back region, the PS BL displacement thickness reduced with increasing burn-back. At 50% span, there was a 55% reduction in δ^*/y_{t1} when comparing Geometry 4 and Geometry 1. This was due to a reduced wetted surface (material removed) and greater acceleration rate (shorter surface length; see Fig. 14).

(2) Outside the burn-back region, the PS BL displacement thickness increased slightly with increasing burn-back. At 5% and 95% span, δ^*/y_{t1} was 23% and 70% greater—respectively—for Geometry 4 than for Geometry 1. This is a small effect, but hard to explain: there is very little change in either the PS loading (see Fig. 14) or the surface streamline pattern in the near-endwall region (see Fig. 11). The increase may arise because of a slight increase in TE Mach number very local to the TE.

(3) On the SS in the near-endwall regions (5% and 95% span) the BL displacement thickness reduced with increasing burn-back. At 5% and 95% span, δ^*/y_{t1} was 56% and 50% lower —respectively—for Geometry 4 than for Geometry 1. The reduction in BL thickness appears to be due to local divergence of vane surface streamlines, caused by fluid migration towards midspan (see Fig. 11).

(4) On the SS away from the endwall (25%, 50%, and 75% span) the effect was inverted and the BL thickened with an increasing cut-back, due to the increasing strength of adverse pressure gradient in the approach to the TE (possible weak shock, see Fig. 14). At 50% span, δ^*/y_{t1} was 118% greater for Geometry 4 than for Geometry 1.

The displacement thicknesses at all five-span locations and for Geometry 1–4 are summarised in the bar chart of Fig. 16. Averaged across the five-span locations, the PS boundary layer displacement thickness decreased by 9.8% in moving from Geometry 1 to Geometry 4. The corresponding change in the SS displacement thickness was an increase of 46.3%. The corresponding changes in momentum thickness (not shown in the figure) were a decrease in the PS by 18.5% and an increase in the SS by 43.5%. As the overall loss is dominated by the SS loss (this surface accounts for 94% of the overall loss), the change in loss is dominated by the increase in SS momentum thickness.

We now estimate the contribution to the overall loss of the PS and SS boundary layers. We define the local KE deficit in the BL (see discussion in Mee et al. [23]), $e_{\mathrm{KE}}(r)$, as the integral of the difference between the actual KE and the KE that the same gas would have had at freestream conditions

$$e_{\mathrm{KE}}(r) = 0.5\int_0^{\delta_{99}} \rho(y, r)u(y, r)[U(r)^2 - u(y, r)^2]dy \qquad (4)$$

where $\rho(y, r)$ and $u(y, r)$ are the local density and velocity as functions of surface-normal distance from the surface at a particular radial location, and $U(r)$ is the velocity at edge of BL at a particular radial location. The integration is performed at the damage front (the location moves upstream as the vane is progressively cut back). Radial distributions $e_{\mathrm{KE}}(r)$ normalised by the maximum value across all simulations, $e_{\mathrm{KE,ref}}$ (i.e., $e_{\mathrm{KE}}(r)/e_{\mathrm{KE,ref}}$) are plotted in Fig. 17 for Geometry 1–4.

Consider first the data for Geometry 1. We see that the SS dominates the boundary layer loss, with the mean value of $e_{\mathrm{KE}}(r)$ for the SS being 15 times that for the PS. In terms of spanwise distribution, both the SS and PS distributions are relatively constant with the span, with some concentration of BL loss on the SS in the peaks at approximately 5% and 90% span corresponding to locations of the hub and case passage vortices (recall vorticity plots in Fig. 7) which roll endwall fluid up into the BL.

With increasing burn-back, we see the following effects:

(1) On the PS, there is a significant decrease (by up to 75% between Geometry 1 and Geometry 4) in loss within the

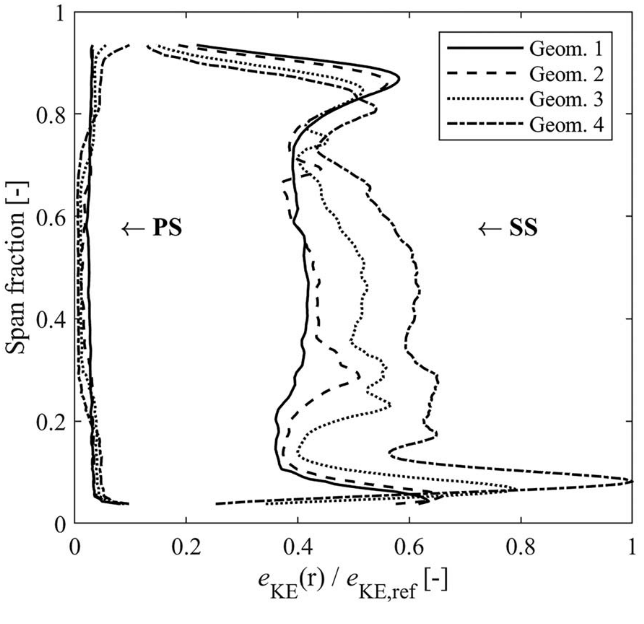

Fig. 17 CFD-predicted spanwise distribution of normalised boundary layer KE dissipation coefficient, e_{KE}, for Geometry 1–4

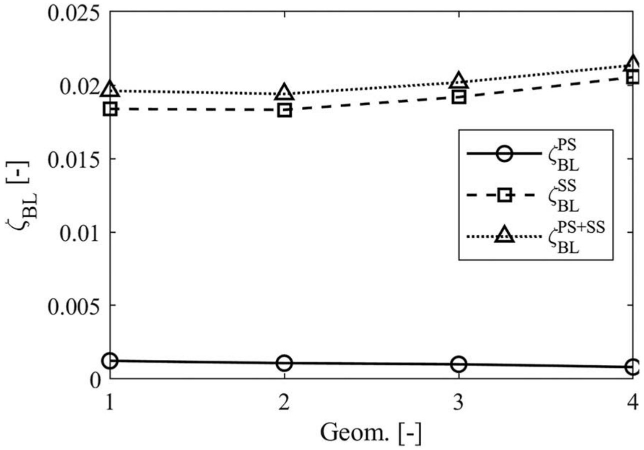

Fig. 18 CFD-predicted BL loss coefficients for Geometry 1–4

burn-back region. This is due to reduced wetted surface and greater acceleration rate (see Fig. 14).

(2) On the SS, the BL loss increases over almost the entire span, with a greater increase near the hub than in the case. This is caused by the significant increase in BL thickness due to increasing adverse pressure gradient on the aft part of the vane (see Fig. 14). The peaks in loss migrate towards midspan (from 4% to 9% span and from 87% to 81% span) leading to slight reductions in loss in the near-wall regions. The migration is explained by the decreased static pressure downstream of TE within the burn-back region, creating local pressure gradients radially inwards.

Now consider the BL loss coefficient (see, for example, Mee et al. [23]) which represents the ratio of KE deficit in the BL at the TE, to the ideal KE flux downstream of the vane if the flow expanded isentropically to the area average static pressure

$$\zeta_{BL} = \frac{\int e_{KE}(r)dr}{\dot{m}_m c_p T_{01}[1 - (\bar{p}_2/p_{01})^X] + \dot{m}_c c_p T_{01}[1 - (\bar{p}_2/p_{0c})^X]} \qquad (5)$$

where $\dot{m}_m$ and $\dot{m}_c$ are the mainstream and coolant mass fluxes, respectively, $\bar{p}_2$ and $\bar{p}_{02}$ are the area-averaged static pressure and the mass-flux-averaged total pressure, respectively, and where p_{0c} is the coolant total pressure at coolant inlet (assumed uniform). T_{01} is the inlet total temperature (same for mainstream and coolant), c_p is the specific heat capacity, and $X = (\gamma - 1)/\gamma$, where γ is the isentropic exponent. The integral and corresponding mass flowrates in the denominator are evaluated between 5% and 95% span.

Evaluating the integral of KE flux dissipation over our set integral limits, we calculate the BL loss coefficients, ζ_{BL}. The PS loss coefficient, ζ_{BL}^{PS}, the SS loss coefficient, ζ_{BL}^{SS}, and the total BL loss coefficient, ζ_{BL}^{PS+SS}, are presented in Fig. 18. With increasing burn-back, the PS BL loss decreases, and the SS BL loss increases. Between Geometry 1 and Geometry 4, the PS BL loss decreases by 34% and the SS BL loss increases by 12%. The total BL loss increases by 9%.

5.7 Coolant Mass Flowrates and Loss With Introduction of Coolant.

We will now consider the impact of TE burn-back on the coolant mass flowrates and associated mixing losses. We find that in the progression from Geometry 1 to Geometry 4 the coolant flow increases for two reasons. First, for fixed inlet total pressure and fixed coolant-to-mainstream total pressure ratio, as the vane Mach number increases, the surface static pressure reduces, driving more flow through the film cooling system. In addition, as the TE slot is cut back, the total pressure requirement to drive flow through the TE circuit reduces, and—separately—there is an increase in the area of the slot. This leads to increased TE coolant flow. Increased cooling flow leads to greater mixing loss. In the particular case of cut-back, our base region increases in area, which—in the absence of other effects—we would expect to increase loss. The change in *overall* loss with the increased cooling flow is a priori uncertain, however, because the total aerodynamic loss is significantly dependent on the TE flow dynamics, which depend on geometry, Mach number, and precise details of coolant ejection (mass flow, angle, etc.) [24], the competing effects are also hard to separate [25], but we can quantify the overall change in loss when coolant is introduced by considering the difference in plane-averaged loss coefficient between cooled and uncooled simulations, i.e., $\Delta\zeta'''_{COOL} = \zeta''' - \zeta'''_{UC}$, where we define the mass-flux-weighted plane-averaged loss coefficient in each case (method 3c in Ref. [15]) by

$$\zeta''' = 1 - \frac{(\dot{m}_m + \dot{m}_c)[1 - (\bar{p}_2/\bar{p}_{02})^X]}{\dot{m}_m[1 - (\bar{p}_2/p_{01})^X] + \dot{m}_c[1 - (\bar{p}_2/p_{0c})^X]} \qquad (6)$$

To reiterate, $\Delta\zeta'''_{COOL}$ is not a mixing loss coefficient, but a change in total loss coefficient when cooling is introduced.

In Table 4, we present (for each build) the coolant mass flow normalised by the Geometry 1 total vane mass flow, $\dot{m}_c/\dot{m}_{total,1}$, and the change in overall loss coefficient with coolant introduction ($\Delta\zeta'''_{COOL}$) as a fraction of the total mass-flux-averaged loss for the uncooled row, i.e., $\Delta\zeta'''_{COOL}/\zeta'''_{UC}$. We also present the percentage increase in these values from the Geometry 1 values.

Table 4 Summary of coolant fraction and overall loss change with coolant introduction for Geometry 1–4

			Δ with respect to Geometry 1 (%)	
Geometry	$\frac{\dot{m}_c}{\dot{m}_{total,1}}$ (%)	$\frac{\Delta\zeta'''_{COOL}}{\zeta'''_{UC}}$ (%)	$\frac{\dot{m}_c}{\dot{m}_{total,1}}$	$\frac{\Delta\zeta'''_{COOL}}{\zeta'''_{UC}}$
1	6.6	12.0	–	–
2	6.7	17.1	+1.8	+42.4
3	7.0	16.0	+6.5	+33.1
4	7.5	20.0	+14.6	+67.0

We find that with increasing burn-back the total coolant mass flowrate increases from 6.6% to 7.5% of the Geometry 1 total vane flow. The additional loss associated with the introduction of coolant flow increases from 12.0% of the uncooled row loss to 20.0% of the uncooled row loss. The change in coolant flow fraction between Geometry 1 and Geometry 4 is 14.6%, but the change in loss increase (with the introduction of coolant) is 67.0%. The disproportionate increase in loss highlights the complexity of the TE flow dynamics, in that there is a different proportional response to cooling flow for different burn-back geometries.

5.8 Overall Aerodynamic Performance.

We will now consider the impact of TE burn-back on overall aerodynamic performance. We consider the plane-averaged loss, ζ''', and mixed-out loss, ζ''''. We also compute the residual secondary kinetic energy (SKE), ζ_{SKE}, at the downstream measurement plane, by difference from the plane-averaged loss and mixed-out loss (i.e., $\zeta_{SKE} = \zeta'''' - \zeta'''$). Conceptually, the residual SKE is the additional loss that would be expected if the flow was allowed to reach its fully mixed state. For the mixed-out loss coefficient (ζ'''') we used the Dzung method (see Ref. [26]; for discussion, see Ref. [15]), in which the flow is mixed to an entirely uniform static pressure defined at a single, swirl-averaged radius

$$\zeta'''' = 1 - \frac{(\dot{m}_m + \dot{m}_c)[1 - (\bar{p}'_2/\bar{p}'_{02})^X]}{\dot{m}_m[1 - (\bar{p}'_2/p_{01})^X] + \dot{m}_c[1 - (\bar{p}'_2/p_{0c})^X]} \qquad (7)$$

where $\bar{p}'_2$ and $\bar{p}'_{02}$ are single values of static and total pressure at the measurement plane computed at nominal radius at which swirl

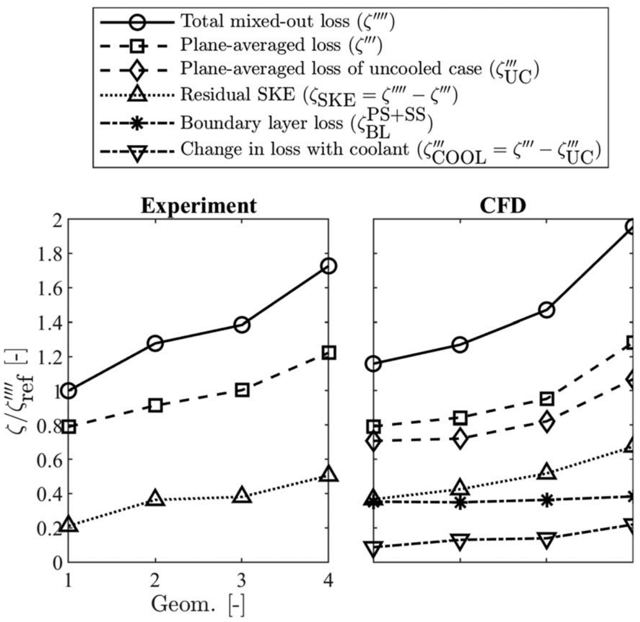

Fig. 19 Coefficients for plane-averaged loss, mixed-out loss, SKE, loss with coolant (compared with uncooled case), and BL loss, for Geometry 1–4 for experiment and CFD predictions

Table 5 Percentage changes (from Geometry 1) in coefficients for: plane-averaged loss, $\Delta\zeta'''$; SKE, $\Delta\zeta_{\mathrm{SKE}}$; mixed-out loss, $\Delta\zeta''''$; BL loss, $\Delta\zeta_{\mathrm{BL}}^{\mathrm{PS+SS}}$; and total loss change with introduction of coolant, $\Delta\zeta'''_{\mathrm{COOL}}$

Geometry	$\Delta\zeta'''$ (%)	$\Delta\zeta_{\mathrm{SKE}}$ (%)	$\Delta\zeta''''$ (%)	$\Delta\zeta_{\mathrm{BL}}^{\mathrm{PS+SS}}$ (%)	$\Delta\zeta'''_{\mathrm{COOL}}$ (%)
Experiment					
1 → 2	+16	+72	+28	–	–
1 → 3	+27	+80	+38	–	–
1 → 4	+55	+140	+73	–	–
CFD					
1 → 2	+7	+16	+10	−1	+50
1 → 3	+20	+41	+27	+3	+61
1 → 4	+62	+84	+69	+9	+153

velocity has its average value. We normalised all loss coefficients by a reference value, ζ''''_{ref}, equal to the value of the Geometry 1 mixed-out loss coefficient.

Normalised plane-averaged loss coefficients, ζ''', mixed-out loss coefficients, ζ'''', and residual SKE coefficients, ζ_{SKE}, for Geometry 1–4 are presented in Fig. 19. Both experimental data and CFD predictions are compared. In the experimental data, the plane-averaged and mixed-out loss coefficients increase monotonically with increasing burn-back, with changes between Geometry 1 and Geometry 4 of 55% and 73% respectively. The SKE also increases monotonically, being 140% greater for Geometry 4 than for Geometry 1, and accounting for 29% of the change in mixed-out loss. The changes ($\Delta\zeta'''$, $\Delta\zeta_{\mathrm{SKE}}$, and $\Delta\zeta''''$) between each build are summarised in Table 5. Corresponding values for CFD predictions are also presented, and characteristics are shown in Fig. 19. The CFD is in excellent qualitative agreement with the experiment, and in reasonable quantitative agreement, particularly for the Geometry 1 to Geometry 4 change.

For the CFD predictions, we also present the change in the total BL (SS + PS) loss coefficient, $\Delta\zeta_{\mathrm{BL}}^{\mathrm{PS+SS}}$, and the loss coefficient associated with the overall change in loss with coolant introduction, $\Delta\zeta'''_{\mathrm{COOL}}$. The total BL loss coefficient increases by 9% between Geometry 1 and Geometry 4, and—because the mixed-out loss is increasing—reduces from making a contribution of 30% to mixed-out loss to 20%. The change in loss with the introduction of coolant increases by 153% between Geometry 1 and Geometry 4. Strictly we should not think of this term as making a *contribution* to overall mixed-out loss, because it is more inseparably part of defining the overall aerodynamics of the part. For completeness, we note that this term is 8% of the mixed-out loss for Geometry 1 and 11% of the mixed-out loss for Geometry 4, however.

In summary, with increasing burn-back, there is little change in the BL loss (decreased wetted surface area near the midspan is offset by increased loading near the endwalls), but there is a significant increase in the plane-averaged loss (increased projected area of the base-pressure region; increased loading; already manifest secondary flow loss as a result of intensified vortices), and a significant increase in SKE (formation of strong pair of vortices at the burn-back edges; strengthening of some preexisting secondary flows). This leads to a significant increase in overall mixed-out loss.

5.9 Impact on Capacity and Stage Performance. The impact of TE burn-back on NGV aerodynamic performance has been discussed. There is also an impact on vane and stage flow capacity, and on the stage aerodynamic performance. The changes from the Geometry 1 NGV capacity are +2.7%, +7.4%, and +16.1% for Geometry 2–4, respectively. These changes are large, and, in conjunction with exit whirl angle changes, have significant impact on inter-stage pressure, and therefore the stage performance. As an example, the changes in stage reaction from Geometry 1 are 3.3%, 8.5%, and 16.2% for Geometry 2–4, respectively; these are large changes that impact the stage work and efficiency. The analysis of why these changes in flow capacity and stage performance exist is complex and clearly a necessary step to develop whole-life engine models and, so, is the subject of future papers.

6 Conclusions

In this paper, we study the impact of TE burn-back on the aerodynamic performance of a high-pressure NGV. We present high-fidelity experimental measurements from an annular cascade operating under engine-matched operating conditions. Fully cooled real-engine parts have been used. The experimental data are complemented with cooled steady RANS of a part with fully resolved TE slot. The parametric burn-back geometries used in the study were derived from statistical analysis of engine deterioration data.

We find the following:

(1) *Damage shape.* Statistical analysis of engine deterioration data showed that the mean damage front centre was close to midspan, with a shape that was somewhat trapezoidal.

(2) *General flow pattern.* With increasing burn-back; a strong pair of counterrotating vortices were introduced at the burn-back edges, which caused increased loss and distortion of the wake; there was under-turning in the burn-back region (change of metal angle) and over-turning outside the burn-back region (increased loading), which led to further distortion of the wake shape, and a significant increase in flow nonuniformity. We found that the CFD method did well at predicting the general flow situation, with some overprediction of peak loss due to underprediction of the mixing rate.

(3) *Exit whirl angle distribution.* Increasing burn-back had a significant impact on the downstream vane exit flow angle distribution, partly as the direct result of TE material removal, but also due to the impact of new secondary flow vortices and vane reloading in response to the material removal. Hub-to-tip whirl angle difference increased from 7.4 deg to

16.4 deg between Geometry 1 and Geometry 4. Local gradients were also significantly increased. This has implications for stage performance, and also rotor design, if acceptable stage performance is required even for deteriorated nozzle parts.

(4) *Boundary layer profiles and loss.* The boundary layer loss accounted for approximately 30% of the overall mixed-out loss for the baseline part, of which approximately 1/10th could be attributed to the PS and 9/10th to the SS. With increasing cut-back, there was a complex redistribution of loss between the burn-back region and the non-burn-back region. The total boundary layer loss increased by 9% for the most extreme burn-back geometry. This change was dominated by the change in the SS boundary layer. With increasing burn-back, the overall vane mixed-out loss increased at a greater rate than the boundary layer loss (formation of new secondary flows), so the BL loss accounted for a smaller proportion of the overall loss.

(5) *Vane loading distribution, coolant flow, and coolant mixing loss.* With increasing TE burn-back the SS Mach number increased (from mild subsonic to mild supersonic). This led to a reduction in surface static pressures, and there was an attendant increase in total coolant mass flowrate from 6.6% to 7.5% of the reference (Geometry 1) total passage flow. That is, the coolant mass flow increased by 14.6%. Using simulations with and without cooling it was shown that the *change in the increase in loss* with the introduction of coolant was 67.0%. This change is significantly larger than the change in coolant mass flowrate, showing that the impact of coolant on overall loss depends on the entire TE flow dynamics, which depend on geometry, Mach number, and precise details of coolant ejection (mass flow, angle, etc.). That is, the coolant mixing loss is perhaps subordinate to other effects.

(6) *Overall aerodynamic performance.* With increasing burn-back, there is very little change in the BL loss (decreased wetted surface area near the midspan is offset by increased loading near the endwalls), but there is a significant increase in the plane-averaged loss (increased projected area of the base-pressure region; increased loading; already manifest secondary flow loss as a result of intensified vortices), and a significant increase in SKE (formation of strong pair of vortices at the burn-back edges; and strengthening of some pre-existing secondary flows). This leads to a significant increase in overall mixed-out loss. Between Geometry 1 and Geometry 4, the mixed-out loss coefficient increased by 72.8%.

We hope this paper will prove a useful reference point for improved quantitative and qualitative understanding of the penalties associated with TE burn-back and help improve whole-life performance assessment.

Acknowledgment

Marcus Meyer (Rolls-Royce Deutschland), Mathias Michaud, and Daniel Burdett (University of Oxford) are thanked for their technical advice.

Conflict of Interest

There are no conflicts of interest.

Data Availability Statement

The authors attest that all data for this study are included in the paper.

Nomenclature

A_{BB} = Burn-back area (mm^2)
A_{ref} = Reference area (mm^2)
C_{t} = Tangential chord length (mm)
C_x = Axial chord length (mm)
c_{p} = Specific heat capacity (J/kg/K)
d = Tangential depth of burn-back (mm)
e_{KE} = Local KE deficit in boundary layer (−)
k = Turbulent kinetic energy (m^2/s^2)
M = Mach number (−)
$\dot{m}$ = Mass flowrate (kg/s)
$\dot{m}_{\mathrm{total,1}}$ = Geometry 1 total vane mass flowrate (kg/s)
p = Pressure (total or static) (Pa)
$\bar{p}$ = Circumferentially averaged pressure (Pa)
$\bar{p}'$ = Mixed-out pressure (Pa)
R^2 = Coefficient of determination (−)
r = Radial position (mm)
Re = Reynolds number (–)
S = Span height (mm)
T = Temperature (K)
Tu = Turbulence intensity (%)
U = Freestream velocity (m/s)
u = Local velocity (m/s)
w_1 = Width of burn-back at TE (mm)
w_2 = Width of burn-back at damage front (mm)
x = Axial position (mm)
y = Surface-normal distance (mm)
y^+ = Non-dimensional wall distance (−)

Greek Symbols

β = Flow turning (or whirl) angle (deg)
β' = Circumferentially averaged whirl angle (deg)
γ = Ratio of specific heat capacities (−)
δ^{99} = Boundary layer thickness (mm)
δ^{*} = Displacement thickness (mm)
$\Delta\zeta'''_{\mathrm{COOL}}$ = Change in plane-averaged KE loss coefficient with the introduction of coolant (−)
ζ' = Local KE loss coefficient (−)
ζ'' = Circumferentially averaged KE loss coefficient (−)
ζ''' = Plane-averaged KE loss coefficient (−)
ζ'''_{UC} = Plane-averaged KE loss coefficient for uncooled simulation (−)
ζ'''' = Mixed-out KE loss coefficient (−)
ζ_{BL} = Boundary layer loss coefficient (−)
$\zeta_{\mathrm{BL}}^{\mathrm{PS}}$ = PS boundary layer loss coefficient (−)
$\zeta_{\mathrm{BL}}^{\mathrm{SS}}$ = SS boundary layer loss coefficient (−)
$\zeta_{\mathrm{BL}}^{\mathrm{PS+SS}}$ = Total boundary layer loss coefficient (−)
ζ_{SKE} = Residual SKE loss coefficient (−)
θ = Momentum thickness (mm)
ρ = Local density (kg/m^3)
X = $(\gamma - 1)/\gamma$
ω = Specific turbulence dissipation rate (1/s)
ω_x = Component of vorticity in axial direction (1/s)

Subscripts

0 = Stagnation condition
1 = Upstream of NGV; Geometry 1
2 = Downstream of NGV; Geometry 2
3 = Geometry 3
4 = Geometry 4
BB = Burn-back region
non-BB = Non-burn-back region
c = Coolant
s = Isentropic condition
m = Mainstream
MAX = Maximum value

MEAN = Mean value
PS = Pressure side
ref = Reference value
SS = Suction side
t = Geometric throat width

References

[1] Sjolander, S. A., Isaacs, D., and Klein, W. A., 1993, "Aerodynamics of Turbine Blades With Trailing-Edge Damage: Measurements and Computations," Proceedings of the International Symposium on Air Breathing Engines 1993, Tokyo, Japan, Sep. 20–24, 1993, Paper No. ISABE93-7130.

[2] Islam, A. M. T., 1999, "An Experimental and Computational Study of the Aerodynamics of Turbine Blades With Damage," Ph.D. thesis, Carleton University, Canada.

[3] Wang, S.-S., Mao, J.-R., Liu, G.-W., and Feng, Z.-P., 2010, "Performance Deterioration of the Governing Stage Nozzle Caused by Solid Particle Erosion in the Steam Turbine," Proc. Inst. Mech. Eng., Part A: J. Power Energy, **224**(2), pp. 279–292.

[4] Bouchard, D., Asghar, A., LaViolette, M., Allan, W. D. E., and Woodason, R., 2014, "Experimental Evaluation of Service-Exposed Nozzle Guide Vane Damage in a Rolls Royce A-250 Gas Turbine," ASME J. Eng. Gas Turbines Power, **136**(10), p. 102601.

[5] Meyer, M., Parchem, R., and Davison, P., 2011, "Prediction of Turbine Rotor Blade Forcing Due to In-Service Stator Vane Trailing Edge Damage," Proceedings of the ASME Turbo Expo 2011, Vancouver, Canada, June 6–10, 2011, Paper No. GT2011-45204.

[6] Di Mare, L., Imregun, M., Smith, A. D., and Elliott, R., 2007, "A Numerical Study of High Pressure Turbine Forced Response in the Presence of Damaged Nozzle Guide Vanes," Aeronaut. J., **111**(1125), pp. 751–757.

[7] Rajput, M. U., 2013, "Evaluation of Experimental Forced Response Data of a Turbine Stage With Respect to Different Stator Blade Damages," M.Sc. thesis, KTH Royal Institute of Technology, Sweden.

[8] Kost, F., and Giess, P. A., 2004, "Experimental Turbine Research at DLR Göttingen," J. Gas Turbine Soc. Japan, **32**(6).

[9] Michaud, M., Jackson, D., Goenaga, F., and Povey, T., 2023, "Experimental Study of Impact of In-Service Deterioration on Aerodynamic Performance of High-Pressure Nozzle Guide Vanes," ASME J. Turbomach., **145**(6), p. 061017.

[10] Michaud, M., Chowdhury, N. H, K., and Povey, T., 2023, "Experimental Study of Impact of In-Service Deterioration on Thermal Performance of High-Pressure Nozzle Guide Vanes," ASME J. Turbomach., **145**(2), p. 021014.

[11] Kirollos, B., Lubbock, R., Beard, P., Goenaga, F., Rawlinson, A., Janke, E., and Povey, T., 2017, "ECAT: An Engine Component Aerothermal Facility at the University of Oxford," Proceedings of ASME Turbo Expo 2017, North Carolina, USA, June 26–30, 2017, Paper No. GT2017-64736.

[12] Messenger, A., and Povey, T., 2020, "Calibrated Low-Order Transient Thermal and Flow Models for Robust Test Facility Design," J. Global Power Propul. Soc., **4**(1), pp. 94–113.

[13] Michaud, M., Ornano, F., and Povey, T., 2022, "Annular Dump Diffuser and Deswirl System for Back-Pressure Control in Engine-Scale Transonic Annular Cascade," ASME J. Turbomach., **145**(4), p. 041006.

[14] Burdett, D., Hambidge, C., and Povey, T., 2020, "Analysis of Ultra-Low Uncertainty Gas Turbine Flow Capacity Measurement Techniques," Proc. Inst. Mech. Eng., Part A:: J. Power Energy, **235**(5), pp. 1053–1079.

[15] Burdett, D., and Povey, T., 2022, "Analysis of Averaging Methods for Nonuniform Total Pressure Fields," ASME J. Turbomach., **144**(5), p. 051011.

[16] Amend, J., and Povey, T., 2024, "Comparison of Eddy Viscosity Models for High Turbulence NGV Flows," ASME J. Turbomach., **146**(8), p. 081004.

[17] Amend, J., Lubbock, R., Ornano, F., Chowdhury, N., and Povey, T., 2024, "Aerodynamic and Thermal Field Development of Cooled Transonic HP NGV," ASME J. Turbomach., **146**(2), p. 021010.

[18] Smith, L. H. Jr., 1966, "The Radial-Equilibrium Equation of Turbomachinery," ASME J. Eng. Power, **88**(1), pp. 1–12.

[19] Rowbury, D., 1998, "Discharge Coefficients of Nozzle Guide Vane Film Cooling Holes," Ph.D. thesis, University of Oxford, England.

[20] Burdett, D., and Povey, T., 2022, "Experimental and Numerical Analysis of Loss Characteristics of Cooled Transonic Nozzle Guide Vanes," ASME J. Turbomach., **144**(5), p. 051009.

[21] Goldstein, R. J., and Spores, R. A., 1988, "Turbulent Transport on the Endwall in the Region Between Adjacent Turbine Blades," ASME J. Heat Transfer, **110**(4a), pp. 862–869.

[22] Mee, D. J., Baines, N. C., and Oldfield, M. L. G., 1992, "Detailed Boundary Layer Measurements on a Transonic Turbine Cascade," ASME J. Turbomach., **114**(1), pp. 163–172.

[23] Mee, D. J., Baines, N. C., Oldfield, M. L. G., and Dickens, T. E., 1992, "An Examination of the Contributions to Loss on a Transonic Turbine Blade in Cascade," ASME J. Turbomach., **114**(1), pp. 155–162.

[24] Melzer, A. P., and Pullan, G., 2019, "The Role of Vortex Shedding in the Trailing Edge Loss of Transonic Turbine Blades," ASME J. Turbomach., **141**(4), p. 041001.

[25] Burdett, D., and Povey, T., 2022, "Impact of Trailing Edge Overhang Length on the Loss Characteristics of Fully Cooled Transonic Nozzle Guide Vanes," ASME J. Turbomach., **145**(5), p. 051012.

[26] Dzung, L. S., 1971, "Konsistente Mittlewerte in der Theorie der Turbomaschinen für Kompressible Medien," BBC Mitt., **58**.